Journal of Materials Chemistry A

Heteroatoms (P, B, S) incorporated NiFe-based nanocubes as efficient electrocatalysts for oxygen evolution reaction

Journal:	*Journal of Materials Chemistry A*
Manuscript ID	TA-ART-01-2018-000410.R1
Article Type:	Paper
Date Submitted by the Author:	05-Mar-2018

Complete List of Authors:	Xuan, Cuijuan; Huazhong University of Science and Technology, School of Chemistry and Chemical Engineering Wang, Jie; Huazhong University of Science and Technology, School of Chemistry and Chemical Engineering Xia, Weiwei; Center for Functional Nanomaterials; Southeast University Zhu, Jing; School of Chemistry and Chemical Engineering, Huazhong University of Science&Technology Peng, Zongkai; Huazhong University of Science and Technology, School of Chemistry and Chemical Engineering Xia, Kedong; Huazhong University of Science and Technology, School of Chemistry and Chemical Engineering Xiao, Weiping; Huazhong University of Science and Technology, School of Chemistry and Chemical Engineering Xin, Huolin L.; Center for Functional Nanomaterials, Wang, Deli; Huazhong University of Science&Technology, School of Chemistry and Chemical Engineering

SCHOLARONE™
Manuscripts

Journal of Materials Chemistry A

ARTICLE

Heteroatoms (P, B, S) incorporated NiFe-based nanocubes as efficient electrocatalysts for oxygen evolution reaction

Received 00th January 20xx,

Accepted 00th January 20xx

DOI: 10.1039/x0xx00000x

www.rsc.org/

Cuijuan Xuan[a], Jie Wang[a], Weiwei Xia[b,c], Jing Zhu[a], Zongkai Peng[a], Kedong Xia[a], Weiping Xiao[a], Huolin L. Xin[b], Deli Wang[a]*

Exploring low-cost and highly-efficient electrocatalysts toward oxygen evolution reaction (OER) is of significant importance, although facing great challenge for the sustainable energy systems. In this work, amorphous NiFe-based porous nanocubes (Ni-Fe-O-P, Ni-Fe-O-B, Ni-Fe-O-S) are successfully synthesized via a simple and cost-effective one-step calcination of Ni-Fe based metal-organic frameworks (MOFs) and heteroatom containing molecules. The resulting three materials maintain well-defined porous nanocube morphology with heteroatom uniformly distributed in the structure. The unique porous structure can effectively provide more active sites and shorten the mass transport distance. Additionally, the introduction of P, B or S can tune the electronic structure, which is favorable for accelerating the charge transfer, and may lead to the formation of the higher average oxidative valence of Ni species during OER process. Benefiting from the above desirable properties, all the three materials exhibit excellent OER electrocatalytic activities and outstanding long-term stability in a home-made zinc air battery. This work not only provides a general approach for the synthesis of high-efficient electrocatalysts based on the earth-abundant elements, but also highlights the potential prospect of MOFs in the energy conversion and storage devices.

Introduction

Developing clean and sustainable energy conversion and storage techniques has gained much attention due to the increasingly severe energy and environmental problems.[1,2] Among the various applications, oxygen evolution reaction (OER), as the half reaction involved in the technologies (e.g. metal-air batteries and water electrocatalysis), plays a pivotal role in the development of these energy devices.[3,4] However, the sluggish reaction kinetics and large overpotentials are the main bottlenecks facing OER which appealed to be addressed.[5] Currently, one of the most effective approaches is to employ high-efficient electrocatalysts to improve the OER performance.[6] Ruthenium (Ru) and iridium (Ir) based noble metal materials, as the benchmarking catalysts for OER, possess highly efficient electrocatalytic activities, but they have been restricted by the prohibitive cost, scarcity, and poor stability.[7] Accordingly, tremendous efforts have been dedicated to explore high-efficient and stable non-precious metal catalysts for OER based on the earth-abundant elements to make those related sustainable energy technologies more practically feasible.

Among numerous non-noble metal catalysts, *3d*-transition metals (TMs) based materials (such as (oxy)hydroxide,[8-10] phosphides,[11,12] sulfide,[13,14] selenide[15,16]) have received far more attention recently due to their cost-effectiveness, abundant reserves, and good stability during OER process. In particular, NiFe-based nanomaterials have been verified to exhibit superior OER electrocatalytic activities in alkaline media, comparable with or even better than Ir- and Ru- based compounds and have been envisioned as one of the most promising candidates for water splitting.[5] Presently, the NiFe based oxides and layered double hydroxide (LDH) have been widely investigated.[17,18] Numerous studies have proposed that the synergy of nickel and iron can modify electronic structure, increase the number of redox reaction sites, and improve the electrical conductivity, hence promoting the OER electrocatalytic activity.[19,20] Additionally, the introduction of heteroatom into TMs-based catalysts, such as forming phosphate[21] and borate,[22] would further tune the electronic structure and facilitate the electron transport in the process of OER.[2,23] Furthermore, catalysts with amorphous structure could often provide much more unsaturated atoms as active sites, which is favorable for the enhancement of catalytic activity.[24] Zhao and co-workers[25] synthesized the amorphous iron-doped nickel phosphate supported on nickel foam which exhibited excellent OER catalytic activities. They proposed that the iron incorporation could tune the electronic structure of local Ni-O environments in nickel phosphate, resulting in the enhanced electrocatalytic activities.[25] Zhang's group[26] reported amorphous-like oxygen-incorporated Ni-Fe-S ultrathin nanosheets supported on Ti plate with high-efficient OER activity. And they argued that amorphous nanosheets structure could expose more active sites and the oxygen incorporation is beneficial for obtaining the proper electronic structure, which are responsible to improving the OER performance.[26] On the other hand, the morphology of the catalyst also plays a significant role in enhancing electrocatalytic performance,[27] especially sphere,[28] nanosheet,[29] nanorod,[12] nanowire,[30] nanobox,[31] etc. Typically, three-dimensional porous architecture could provide highly desirable properties compared with zero-, one-, and two-dimensional structure. The fascinating advantages include offering larger surface area, creating much more fast channels for mass transfer and ion diffusion, and increasing the active sites, thus propitious to improve the OER catalytic

[a] *Key laboratory of Material Chemistry for Energy Conversion and Storage (Huazhong University of Science and Technology), Ministry of Education, Hubei Key Laboratory of Material Chemistry and Service Failure, School of Chemistry and Chemical Engineering, Huazhong University of Science and Technology. E-mail: wangdl81125@hust.edu.cn*

[b] *Center for Functional Nanomaterials, Brookhaven National Laboratory, Upton, NY 11973, USA*

[c] *SEU-FEI Nano-Pico Center, Key Laboratory of MEMS of the Ministry of Education, Southeast University, Nanjing 210096, China*

†Electronic Supplementary Information (ESI) available. See DOI: 10.1039/x0xx00000x

This journal is © The Royal Society of Chemistry 20xx

performance.[27] Notwithstanding the above progress, the investigation of heteroatom containing NiFe-based nanomaterials (such as metal phosphate and borate) with three-dimensional porous structures still remains the initial stage mainly due to the complicated and tedious synthesis methods usually required. Besides, it is really essential to explore a synthetic method to obtain Ni-Fe based compounds with heteroatoms doping and study the structure-activity relationship.

Recently, Metal-organic frameworks (MOFs) based derivatives have drawn considerable attention and shown great potential prospects in the energy conversion and storage applications due to the appealing properties such as well-defined three-dimensional structure, large specific surface area, and high porosity.[32-34] In this work, amorphous-like heteroatoms (e.g. P, B, S) containing NiFe-based porous nanocubes (Ni-Fe-O-P, Ni-Fe-O-B, Ni-Fe-O-S) derived from nickel iron Prussian blue analogue (NiFe-PBA) were successfully synthesized through a simple one-step calcination method. NiFe-PBA was employed as the template for the formation of three-dimensional porous structure, while small molecules (e.g. ammonium dihydrogen phosphate, boric acid, thiourea) serve as P, B and S sources for the introduction of heteroatom. The as-prepared materials maintained well-defined porous nanocube structure with heteroatom uniformly distributed in the structure. Electrochemical results demonstrate that the resulting catalysts all exhibit superior electrocatalytic activities and outstanding long-term stability toward OER in alkaline media, even much better than Ir/C. Besides, the three electrocatalysts also show excellent rate capability at different current densities and exceptional stability when used in a home-made zinc air battery.

Experimental

Material synthesis

NiFe-based nanocubes containing different heteroatoms (i.e. P, B or S) were synthesized as follows. Firstly, the MOFs (NiFe-PBA) precursors were prepared through a coprecipitation method.[35] Typically, nickel chloride hexahydrate (0.6 mmol) and tri-sodium citrate dihydrate (0.9 mmol) were dissolved in 20 mL of deionized water, and the 0.4 mmol of potassium ferricyanide was dissolved in 20 mL of deionized water. Then, the above two solutions were mixed together under continuous magnetic stirring followed by aging at room temperature for 10 h. The precipitate were collected after centrifugation and washed using water and ethanol for several times. After dried overnight at 60 °C. the resulting NiFe-PBA (40 mg) was ground with 0.2 mmol of $NH_4H_2PO_4$, H_3BO_3, or thiourea, respectively, and then heated up to 450 °C in air for 5 h with a heating rate of 3 °C min^{-1} to obtain the final products, which denoted as Ni-Fe-O-P, Ni-Fe-O-B, and Ni-Fe-O-S, respectively. For comparison, Ni-Fe-O without heteroatoms was prepared by direct annealing of NiFe-PBA precursor in air with the same temperature and heating procedures.

Material characterization

The scanning electron microscopy was conducted via field emission scanning electron microscopy (FESEM, Sirion200). Transmission electron microscopy (TEM), scanning transmission electron microscopy (S-TEM) and elemental mapping images were acquired on a Tecnai G2 F30. Powder X-ray diffraction (XRD) determination was performed on an X'Pert PRO diffractometer. Fourier transform infrared spectroscopy (FTIR) was characterized at ambient temperature with a FTIR spectrometer (VERTEX 70, BRUKER Inc.). Inductively coupled plasma atomic emission spectroscopy (ICP-AES) was detected by an IRIS Advantage spectrometer (Thermo Elemental Co. USA). X-ray photoelectron spectroscopy (XPS) detection was performed employing an AXIS-ULTRA DLD-600W Instrument. X-ray Fluorescence (XRF) measurements were conducted on an EAGLE III spectrometer. N_2 adsorption-desorption isotherms, Brunauer-Emmett-Teller (BET) surface area, and pore distribution were detected by using ASAP2420-4MP analyzer.

Electrochemical measurement

Electrochemical workstation (Autolab PG302N) equipped with high-speed rotators from Pine Instrument was utilized for all the electrochemical measurements. During the electrochemical process, the three-electrode setup was employed in which glassy carbon electrode (GCE) with a diameter of 5 mm, carbon rod and the reverse hydrogen electrode were employed as working electrode, counter electrode and reference electrode, respectively. The working electrode loaded with catalysts was prepared according to the drip-coating method. Specifically, 5 mg of sample and 2 mg of Vulcan XC-72 were first mixed with 1 mL Nafion/isopropyl alcohol mixed solution to acquire the homogeneous ink dispersion; and then, the obtained ink (16.5 μL) was dropped onto the working electrode and dried at room temperature naturally with the catalyst loading amount of about 0.42 mg cm^{-2}. The working electrode loaded with Ir/C catalyst was prepared based on the same procedure with the loading amount of 0.08 mg cm^{-2}. The OER performance was measured in 1M KOH solution. Cyclic voltammetry (CV) and linear sweep voltammetry (LSV) measurements were carried out at the scan rate of 50 mV s^{-1} and 5 mV s^{-1}, respectively, at the potential ranging from 0.8 V to 1.8 V vs. RHE. Electrochemical impedance spectroscopy (EIS) data were recorded at 1.5 V in the frequency range from 100 kHz to 0.01 Hz with an ac perturbation of 5 mV. Chronoamperometry detection was realized at the current density of 10 mA cm^{-2} or 20 mA cm^{-2} for 10 h with a rotation speed of 1600 rpm to evaluate the stability of the catalysts. Potential cycling ranging from 1.4 V to 1.8 V vs. RHE was also detected to investigate the OER stability.

The rechargeable performance for Zn-air battery was assessed in the home-built two-electrode electrochemical cell. The catalyst loaded on the gas diffusion layer (1 cm^2, catalyst loading 1 mg cm^{-2}) and the pre-polished Zn foil served as air cathode and anode, respectively, with 6 M KOH solution containing 0.2 M $Zn(CH_3COO)_2$ as electrolyte. As for the preparation of gas diffusion layer, Vulcan XC-72 (400 mg), PTFE (100 mg) and moderate isopropanol were milled fully in agate mortar, then the obtained homogenous slurry was pressed by a twin roller to get a composite sheet. After drying under vacuum for overnight, the resulting sheet was tailored into suitable size to spare. During the battery detection process, air was continuously fed to the cathode. And the discharge/charge performance was measured on the LAND-CT2001A testing devices. The stability test was conducted by discharging/charging determination at a current density of 10 mA cm^{-2} with each cycle being 1 h.

Results and discussion

The synthesis of amorphous Ni-Fe-O-H (H = P, B, or S) nanocubes with porous structure was accomplished through a simple two-step method, as displayed in Scheme 1. Firstly, NiFe-PBA nanocubes were prepared via the coprecipitation of nickel chloride hexahydrate with potassium ferricyanide. NiFe-PBA particles exhibit smooth surface with well-defined uniform nanocube shape with an average size ranging from 100 to 150 nm (Figure 1a and b). Besides, the TEM image in Figure 1c clearly illustrated the solid and dense cubic structure of the MOF without discernable pores. The XRD patterns in Figure 1d indicated NiFe-PBA presents the well crystallinity characterising the typical diffractions of face-center-cubic structure (**$Ni_3[(FeCN)_6]_2 \cdot 10H_2O$**, JCPDS card 46-0906**)** and no other impurity peaks were detected, revealing the successful preparation of pure MOFs.

This journal is © The Royal Society of Chemistry 20xx

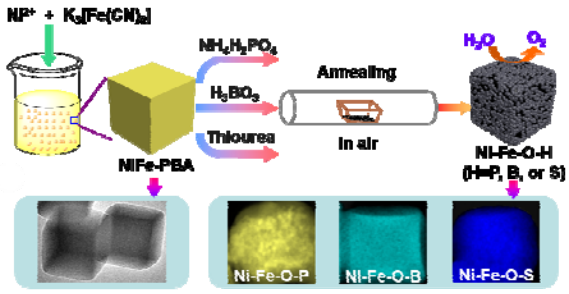

Figure 1 Schematic illustration for the synthesis of Ni-Fe-P-H catalysts.

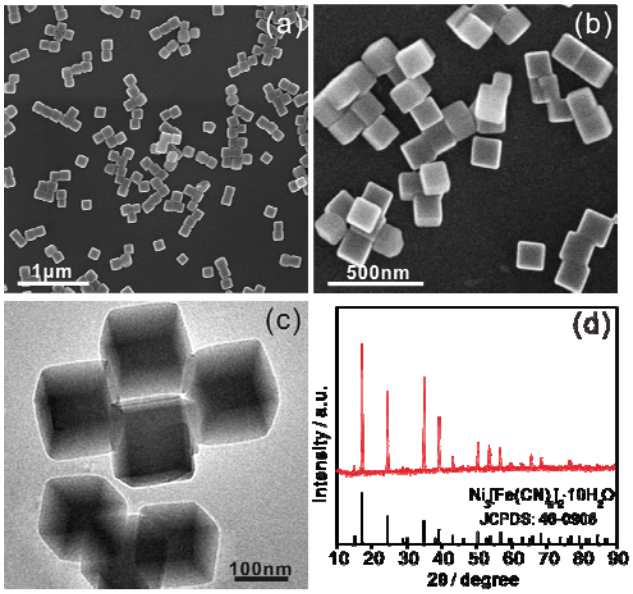

Figure 1 SEM (a, b) and TEM (c) images of NiFe-PBA. XRD patterns (d) of NiFe-PBA.

The NiFe-PBA in the presence of heteroatom precursors were subjected to the thermal treatment (Scheme 1), forming amorphous Ni-Fe-O-H (H= P, B, or S) (Figure S 1a). In contrast, the sample obtained by direct oxidation of NiFe-PBA exhibits typical diffraction peaks of NiO (JCPDS card 47-1049) and $NiFe_2O_4$ (JCPDS card 54-0964). These observations suggested that the MOF precursor would preferentially react with both small molecule and oxygen for the formation of amorphous materials. Compared with crystalline structure, the samples with amorphous structure have been proposed to achieve enhanced catalytic activity benefiting from the much more active sites.[27] The chemical structure of the MOF precursor and its derived materials was further examined through the Fourier transform infrared (FT-IR) spectroscopy. Figure S1b clearly presented the characteristic peaks of water molecules (~ 3408 cm^{-1} and ~1611 cm^{-1}) and CN group (2158.2 cm^{-1} and 2113.5 cm^{-1}) of NiFe-PBA.[36,37] Upon thermal treatment, these typical bonds could not be detected, demonstrating the entire decomposition of MOFs. SEM and TEM measurements were then performed to manifest the morphology of the as-prepared Ni-Fe-O-H. As indicated Figure S2, the resulting Ni-Fe-O-H products all well inherited the nanocube architecture. Consistent with the SEM images, STEM and TEM images in Figure 2 clearly showed the well-defined nanocubic morphology of Ni-Fe-O-H with much rough surface. Besides, the porous architecture of Ni-Fe-O-H could be obviously observed, providing large amounts of pores and channels for mass transfer and ion diffusion. Compared with Ni-Fe-O-B and Ni-Fe-O-S, Ni-Fe-O-P exhibits more pores, implying direct annealing NiFe-PBA and $NH_4H_2PO_4$ of lead to the easier formation of porous structure. The elemental mapping in Figure 2d confirmed the successful incorporation of P and the uniform distribution of Ni, Fe, P, and O in Ni-Fe-O-P nanomaterial. Similar phenomenon was also observed in Ni-Fe-O-B and Ni-Fe-O-S samples. As revealed in Figure 2h and l, B and S have been successfully incorporated, respectively, indicating a partial reaction between MOFs and heteroatom containing molecules. Meanwhile, it could be clearly presented that Ni, Fe, B, and O elements were uniformly distributed across the whole Ni-Fe-O-B nanocube particles, and the Ni-Fe-O-S sample exhibited the homogeneous scattering of Ni, Fe, S, and O elements. Besides, the atomic ratio of Ni, Fe, and P (or B, S) was determined by ICP-AES measurements with 1.50:1:1.64 for Ni-Fe-O-P, 1.49:1:2.15 for Ni-Fe-O-B, and 1.50:1:0.71 for Ni-Fe-O-S. In order to further illustrate the porous structure of the catalysts, Brunauer-Emmett-Teller (BET) surface area and pore size distribution of Ni-Fe-O-P, Ni-Fe-O-B, Ni-Fe-O-S, and Ni-Fe-O materials were examined. The N_2 adsorption-desorption isotherms and pore distribution are shown in Figure S3. Compared with Ni-Fe-O-B, Ni-Fe-O-S, and Ni-Fe-O catalysts, Ni-Fe-O-P materials exhibit a type IV N_2 adsorption-desorption isotherms with an H2 hysteresis loop and also show a large number of mesopores in pore distribution, revealing the mesoporous feature of Ni-Fe-O-P, consistent with TEM images. The BET surface area of Ni-Fe-O-P, Ni-Fe-O-B, Ni-Fe-O-S, and Ni-Fe-O catalysts is determined to be 78.5 m^2 g^{-1}, 29.5 m^2 g^{-1}, 28.1 m^2 g^{-1}, 39.1 m^2 g^{-1}, respectively, demonstrating Ni-Fe-O-P possesses a larger surface area which is favorable for the improvement of catalytic activities.

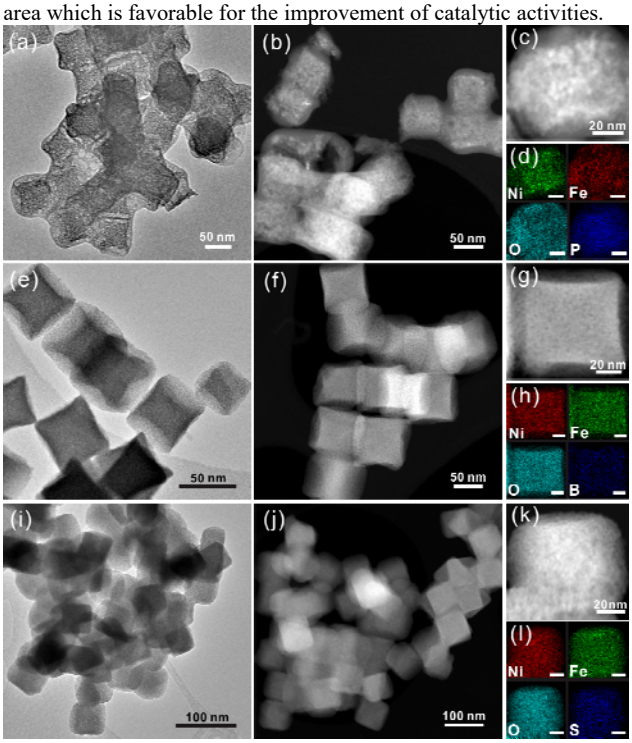

Figure 2 TEM (a) and STEM (b) images of Ni-Fe-O-P. Enlarged STEM image (c) and the corresponding elemental mapping of Ni, Fe, O, and P (d). TEM (e) and STEM (f) images of Ni-Fe-O-B; Enlarged STEM image (g) and the corresponding elemental mapping of Ni, Fe, O, and B (h). TEM (i) and STEM (j) images of Ni-Fe-O-S; Enlarged STEM image (k) and the corresponding elemental mapping of Ni, Fe, O, and S (l). The scale bar in (d, h, l) is 20 nm.

The surface chemical compositions and elemental valence states of the Ni-Fe-O-H materials were assessed by X-ray photoelectron spectroscopy (XPS) measurement. The XPS survey spectrum in Figure S4 obviously indicated the presence of Ni, Fe, O and P, B, S, further confirming the successful incorporation of P, B, S in Ni-Fe-O-P, Ni-Fe-O-B, Ni-Fe-O-S, respectively, consistent with the elemental mapping images. For Ni-Fe-O-P, the high-resolution spectra of Fe 2p, Ni 2p, P 2p are presented in Figure 3 a-c. In Ni 2p region (Figure 3a), the binding energies appeared at 857.3 eV (Ni 2p3/2) and 875.0 eV (Ni 2p1/3) as well as the corresponding satellite peaks at 862.4 eV and 880.4 eV, revealed the formation of oxidized nickel species.[38,39] The high-resolution core spectrum of Fe 2p (Figure 3b) displayed two peaks located at 713.2 eV (Fe 2p 3/2) and 726.9 eV (Fe 2p1/2) along with the satellite peak at 719.0 eV, confirming the presence of the oxidation state of iron with Fe^{3+} as the primary existence form.[25,40,41] The peak at 133.7 eV in the high-resolution P 2p spectrum (Figure 3c) could be attributed to the P-O bonding, suggesting the generation of phosphate species.[42,43] For Ni-Fe-O-B, as depicted in Figure 3a, the high-resolution of Ni 2p showed two peaks located at 856.0 eV (Ni 2p 3/2) and 873.8 eV (Ni 2p1/2), with two satellite peaks at 862.1 eV and 880.1 eV, demonstrating nickel species with oxidation state were formed.[39,44] The Fe 2p region in Figure 3b exhibited three peaks at binding energies of 712.1 eV, 718.5 eV and 725.7 eV, assigned to the Fe 2p1/2, Fe 2p3/2 core levels as well as satellite peak, illustrating the generation of Fe species with high oxidation state (Fe^{3+}).[40,41] The high-resolution B 1s spectrum (Figure 3d) displayed the peak located at 191.8 eV, revealing the presence of B-O bonding and the existence of borate.[45] As for Ni 2p in Ni-Fe-O-S, four peaks were observed as shown in Figure 3a. The binding energies at 856.5 eV and 874.1 eV could be ascribed to the signals of Ni 2p3/2 and Ni 2p1/2, respectively. The other two peaks at 862.4 eV and 880.5 eV corresponded to the satellite peaks, indicating the existence of oxidized Ni species.[39] The three peaks at 712.7 eV, 726.2 eV and 718.9 eV (Figure 3b) could be assigned to the Fe 2p1/2, Fe 2p3/2 as well as the satellite peak, respectively, manifesting the formation of iron with the high oxidation state (Fe^{3+}).[40,41] The high-resolution of S 2p spectrum (Figure 3e) showed two peaks at the binding energy of 168.6 eV and 169.9 eV, suggesting the presence of S-O bonding in Ni-Fe-O-S.[46] All of these observations elucidate the generation of metal phosphate, metal borate as well as metal sulfate in Ni-Fe-O-P, Ni-Fe-O-B, Ni-Fe-O-S, respectively, through direct annealing the Ni-Fe-PBA precursor at the presence of $NH_4H_2PO_4$, H_3BO_3 and thiourea.

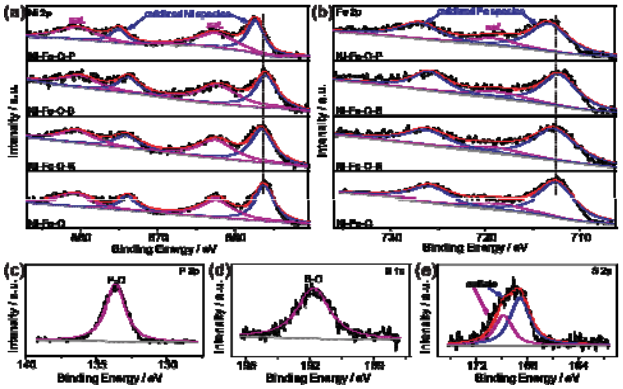

Figure 3 High-resolution XPS spectra of Ni 2p (a), Fe 2p (b) for Ni-Fe-O-P, Ni-Fe-O-B, Ni-Fe-O-S, and Ni-Fe-O. High-resolution XPS spectra of P 2p (c) for Ni-Fe-O-P. High-resolution XPS spectra of B 1s (d) for Ni-Fe-O-B. High-resolution XPS spectra of S 2p (e) for Ni-Fe-O-S.

Additionally, it can be clearly seen from Figure 3 that compared with Ni-Fe-O, P, B, and S incorporation served as the pivotal part in tuning the electronic structure of Ni and Fe elements. As for Ni-Fe-O-P, the binding energies of Ni 2p3/2 and Fe 2p3/2 in the high-resolution XPS spectra showed slight positive shifts after reacted with P containing resources compared with those counterparts in Ni-Fe-O. The similar phenomenon has appeared in Ni-Fe-O-S with the binding energies positive shift for Ni and Fe. For Ni-Fe-O-B, negative shift were observed in the binding energies of Ni and Fe, probably due to the lower electronegativity of boron atom. The shifting of bind energies indicates the modulated electronic structure around Ni and Fe environment, favorable for the electron transport during the electrocatalytic process.

Notably, transition metal phosphate and borate, such as cobalt phosphate,[47] cobalt borate,[48] nickel borate,[44] iron phosphate-borate,[49] have been reported as efficient electrocatalysts due to the low-cost, high intrinsic activity as well as good stability. Some researchers found that the existence of Co^{4+} in cobalt phosphate[50] and the oxidation of average valence state of Ni in nickel borate under the positive potential[51] are responsible to the high-efficient OER electrocatalysis. Moreover, the phosphate group can serve as the proton acceptors, facilitating the oxidation of metal in metal phosphates,[52] and could also lead to the distorted local cobalt geometry with open coordinate site, benefiting for the absorption of reactants.[53] Besides, the edge-sharing CoO_6, NiO_6, and the NiOOH formed during OER process have been proposed to be the active sites for OER.[25,54] Despite the few reports related to the application of metal sulfate in OER, it could be deduced from the researches about metal phosphate and borate that the existence of sulfate group is conducive to the formation of nickel species with higher oxidation state at applied positive voltage. Besides, the electrocatalysts consisting of sulfate would in-situ generate much more defects as active sites that favoring the OER catalytic activity with the dissolution of sulfate.[46] According to the aforementioned characterizations and analysis, it is reasonable to expect that the as-prepared Ni-Fe-O-H (H= P, B, S) would exhibit excellent electrocatalytic activities toward OER benefiting from the unique 3D porous nanocubes, and the amorphous features containing Ni and Fe, as well as the existence of phosphate, borate, or sulfate group.

To evaluate the electrocatalytic performance of the as-synthesized Ni-Fe-O-H nanomaterials, three-electrode configuration was employed by using 1 M KOH as electrolyte. The obtained electrochemical data were calibrated with IR drop compensation. Cyclic voltammogram (CV) curves in Figure 4a clearly presented the unconspicuous anodic peak and notable cathodic peak of Ni-Fe-O-H, implying the oxidation and reduction of Ni (II), in sharp contrast to the negligible redox peaks on Ni-Fe-O. The anodic wave was not obviously observed, which could be ascribed to the overlapping with the OER current.[17] The appearance of anodic peaks could be ascribed to the formation of NiOOH which is generally considered as the OER active sites and would undergo deprotonation to evolve oxygen.[17,25] Compared with Ni-Fe-O, the remarkable redox peaks of Ni-Fe-O-H demonstrates that incorporating P, B or S could tune the redox properties of Ni species, hence promoting the electron transport and improving the OER activities. The linear sweep voltammetry (LSV) measurements were then carried out at a scan rate of 5 mV s^{-1} with a rotation speed of 1600 rpm. The overpotentials required at current density of 10 mA cm^{-2} (η_{10}) and 20 mA cm^{-2} (η_{20}) were obtained from LSV curves to evaluate the OER activities. As shown in Figure 4b and c, Ni-Fe-O-P, Ni-Fe-O-B, Ni-Fe-O-S exhibit exceptional electrocatalytic activities for OER with lower values of η_{10} and η_{20} (227 mV and 254 mV for Ni-Fe-O-P, 243 mV and 261 mV for Ni-Fe-O-B, 272 mV and 287 mV for Ni-Fe-O-S, respectively). The values of η_{10} and η_{20} are smaller than on Ni-Fe-O (356 mV and 374 mV) and even Ir/C (326 mV and 345 mV), as well as many reported NiFe-based catalysts (Table S1). Compared

This journal is © The Royal Society of Chemistry 20xx

with Ni-Fe-O, the excellent OER activities of Ni-Fe-O-H confirmed the respective introduction of P, B, or S in the form of phosphate, borate, or sulfate as well as the porous structure are favorable for the enhancement of the OER activities.

In order to demonstrate the kinetics for OER, Tafel plot was then obtained from the LSV curves in Figure 4b based on the Tafel equation $\eta=b \log (j/j_0)$, where η represents the overpotential, b is the Tafel slope, j is the current density, and j_0 represents the exchange current density.[55] As revealed in Figure 4d, the values of Tafel slopes on Ni-Fe-O-P, Ni-Fe-O-B, and Ni-Fe-O-S catalysts are 50 mV dec^{-1}, 53 mV dec^{-1}, as well as 70 mV dec^{-1}, respectively. All the values are lower than that on Ni-Fe-O (77 mV dec^{-1}), indicating the improved reaction kinetic rates during OER process. Besides, electrochemical impedance spectroscopy (EIS) was measured on Ni-Fe-O-H materials to further illustrate the OER kinetics and charge transfer process. The Nyquist plots in Figure S5 presented that the three catalysts all exhibited a semicircle in the high frequency range, and the radius of the semicircle represents the charge transfer resistance (R_{ct}), indicating the nature electronic-conductivity of the samples.[56] Clearly, all the Ni-Fe-O-H catalysts exhibited much lower R_{ct} than Ni-Fe-O, implying faster electron-transfer rate during the OER process. Moreover, Ni-Fe-O-P and Ni-Fe-O-B catalysts exhibited lower Tafel slope, and smaller R_{ct} compared with Ni-Fe-O-S material (Figure 4d and S5), further demonstrating the more favorable function of larger surface area and introduction of P for Ni-Fe-O-P as well as the introduction of B for Ni-Fe-O-B in achieving the faster OER kinetics, accelerating electron transfer rate, and hence improving the OER catalytic activities. It could be further seen from Figure S6, S7 and S8 that Ni-Fe-O-H exhibited decreased catalytic activities when higher or lower the amount of small molecule added ($NH_4H_2PO_4$, H_3BO_3, or thiourea) or post-annealing temperature used. And the Ni-Fe-O-H exhibited the best catalytic activities when synthesized by adding 0.2 mmol of $NH_4H_2PO_4$, H_3BO_3, or thiourea respectively, with post-annealing treatment at 450 °C due to the resulting unique well-defined structure and composition under this condition.

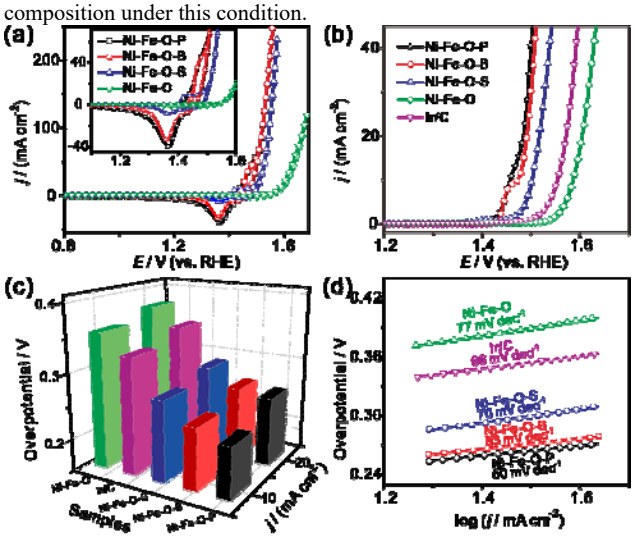

Figure 4 (a) CV curves of Ni-Fe-O-P, Ni-Fe-O-B, Ni-Fe-O-S, and Ni-Fe-O at a scan rate of 50 mV s^{-1}. (b) LSV curves of Ni-Fe-O-P, Ni-Fe-O-B, Ni-Fe-O-S, Ni-Fe-O, and Ir/C at a scan rate of 5 mV s^{-1}, and (c) the corresponding overpotentials for delivering the current densities of 10 mA cm^{-2} and 20 mA cm^{-2}. (d) Tafel slopes of Ni-Fe-O-P, Ni-Fe-O-B, Ni-Fe-O-S, Ni-Fe-O, and Ir/C.

Collectively, the electrochemical results confirm that the as-prepared Ni-Fe-O-P, Ni-Fe-O-B, and Ni-Fe-O-S exhibit excellent electrocatalytic activities toward OER. Combined with the other characterizations discussed above, it can be concluded that the excellent OER activities of these three catalysts could be mainly originated from the following aspects: (i) The presence of P, B, or S can tune the electronic structure around Ni and Fe, which is favorable for expediting the charge-transfer process as manifested from the XPS results with the shifts of binding energies and EIS data with smaller charge-transfer resistances compared with Ni-Fe-O, and also might lead to generating higher average oxidation state of nickel in Ni-Fe-O-H materials, thus promoting the water oxidation reaction.[19,5723,25,44,58] (ii) The unique porous cubic architecture provides maximum active sites with the sufficient contact between catalysts and electrolyte. Besides, the porous structure facilitates the mass transfer and ion diffusion by providing multiple fast channels, and also favor the exposure of more active sites. (iii) The amorphous structure could provide unsaturated atoms as active sites, leading to the increase of active sites as well as the improvement of catalytic activity.[24,25].

The durability of the as-prepared Ni-Fe-O-H catalysts was evaluated by both CV cycling and chronopotentiometry measurements. The chronopotentiometry tests in Figure 5a-c demonstrated the excellent long-term stability of Ni-Fe-O-H catalysts with little activity loss after 10 h at current density of 10 mA cm^{-2} and 20 mA cm^{-2}, respectively. X-ray Fluorescence (XRF) characterization was conducted to illustrate atomic ratio of Ni and Fe for the Ni-Fe-O-H catalyst before and after the stability test. As shown in Figure S9, the atomic ratios of Fe and Ni for initial Ni-Fe-O-H catalysts before stability were about 1.5:1, consistent with ICP-AES results. Compared with the initial state, the atomic ratios of Fe and Ni for Ni-Fe-O-H catalysts after stability test showed a slight drop, demonstrating the good stability of Ni-Fe-O-H. Moreover, Figure 5d depicted that LSV curves of Ni-Fe-O-P, Ni-Fe-O-B, and Ni-Fe-O-S showed negligible current decay after 3000 CV cycles at potential ranging from 1.4 to 1.8 V, further implying the excellent activity retaining ability of Ni-Fe-O-H.

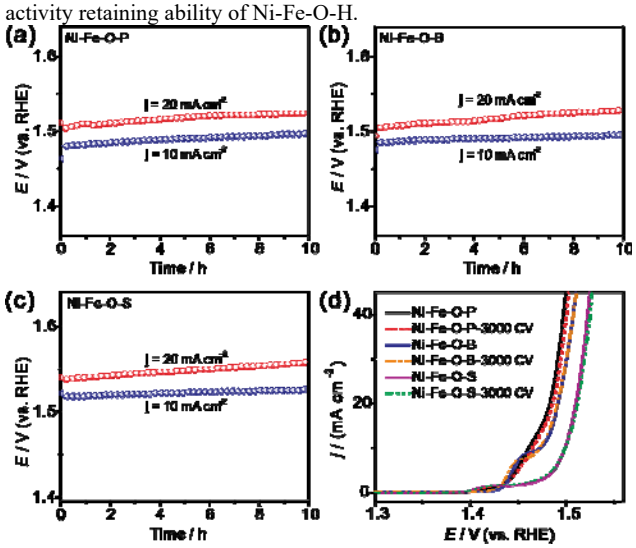

Figure 5 Chronopotentiometry curves of Ni-Fe-O-P (a), Ni-Fe-O-B (b), and Ni-Fe-O-S (c), at a constant current density of 10 mA cm^{-2} and 20 mA cm^{-2}; (d) The OER polarization curves of Ni-Fe-O-P, Ni-Fe-O-B, and Ni-Fe-O-S before and after 3000 CV cycles in the potential range from 1.4 V to 1.8 V.

Based on the excellent OER performance in the three-electrode system, the potential application of the as-prepared Ni-Fe-O-H materials in Zn-air battery was also assessed using the home-made configuration. The air cathode was prepared by mixing the as-prepared Ni-Fe-O-P (or B, S) and the previously reported N,S-CNT with excellent ORR performance[59] since Zn-air battery involves two

reactions of oxygen reduction and oxygen evolution. The polarization curves were detected and used to acquire the corresponding power density. As displayed in Figure 6b, the peak power densities of Ni-Fe-O-P+N,S-CNT, Ni-Fe-O-B+N,S-CNT, and Ni-Fe-O-S+N,S-CNT was 141.4, 145, and 146.3 mW cm^{-2}, respectively, superior to that of Pt/C+Ir/C (108.8 mW cm^{-2}). Then the discharge-charge cycling curves of various catalysts at a current density of 10 mA cm^{-2} were recorded to validate the long-term stability of the catalysts in a Zn-air battery. The voltage profile in Figure 6c depicted that the discharging and charging voltage of Ni-Fe-O-H+N,S-CNT based batteries underwent negligible changes after 100 cycles, whereas a much worse scenario was observed for the Pt/C+Ir/C-based cell with dramatically decreased discharge voltage and increased charge voltage after 60 cycles, which manifested the outstanding stability of Ni-Fe-O-H+N,S-CNT in Zn-air battery. Moreover, Ni-Fe-O-H+N,S-CNT based cells all displayed more stable discharge and charge voltages even after 400 cycles than Pt/C+Ir/C, further demonstrating their excellent durability when used as electrocatalysts for Zn-air batteries. The superior electrocatalytic performances of Ni-Fe-O-H materials with advantages of low cost and easy preparation demonstrate the potential applicability and the promising prospects of Ni-Fe-O-H catalysts in energy conversion and storage devices.

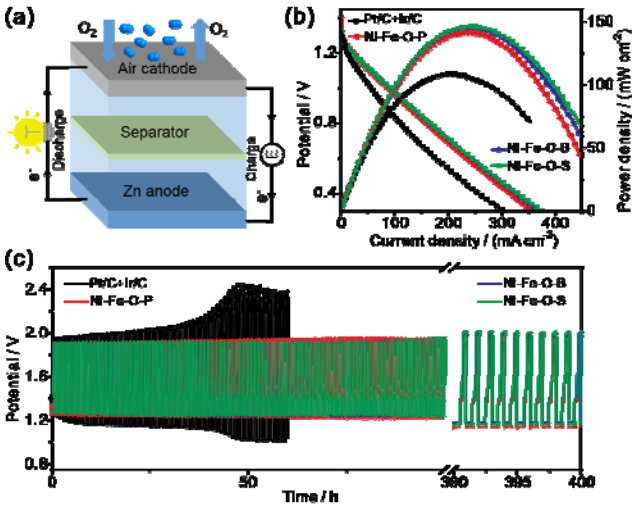

Figure 6 (a) Schematic diagram of zinc-air battery device. (b) Polarization and power density curves of Zn-air batteries with Pt/C+Ir/C, Ni-Fe-O-P+N,S-CNT, Ni-Fe-O-B+N,S-CNT, and Ni-Fe-O-S+N,S-CNT as air cathode, respectively. (C) Discharge/charge cycling curves of Zn-air battery using Pt/C+Ir/C, Ni-Fe-O-P+N,S-CNT, Ni-Fe-O-B+N,S-CNT, and Ni-Fe-O-S+N,S-CNT as air electrode catalysts at a current density of 10 mA cm^{-2}.

Conclusions

In conclusion, amorphous NiFe-based porous nanocubes (Ni-Fe-O-P, Ni-Fe-O-B, Ni-Fe-O-S) were successfully synthesized via a simple one-step calcination of metal-organic frameworks (MOFs) with small heteroatom containing molecules. The resulting materials inherited the advantages of MOFs, exhibiting three-dimensional porous nanocubes, which is favorable for shortening the transport distance of ion and exposing more active sites. Besides, the introduction of P, B or S can effectively tune the electronic structure, which is favorable for accelerating the charge transfer , and may lead to the generation of the higher average oxidation state of Ni species during OER process. All the three materials show excellent electrocatalytic activities and remarkable long-term durability toward OER, even much better than Ir/C, benefiting from the unique structure and composition. Furthermore, when used in the homemade zinc-air battery, the three catalysts exhibit outstanding stability, showing great potential in energy conversion and storage applications.

Acknowledgements

This work was supported by the National Natural Science Foundation (21573083), 1000 Young Talent (to Deli Wang), and the Innovation Research Funds of Huazhong University of Science and Technology (2017KFYXJJ164). The authors thank the Analytical and Testing Center of HUST for allowing use its facilities. This research used resources of the Center for Functional Nanomaterials, which is a U.S. DOE Office of Science Facility, at Brookhaven National Laboratory under Contract No. DE-SC0012704.

Notes and references

1 M. S. Faber and S. Jin, *Energy Environ. Sci.*, 2014, **7**, 3519-3542.
2 S. Anantharaj, S. R. Ede, K. Sakthikumar, K. Karthick, S. Mishra and S. Kundu, *ACS Catal.*, 2016, **6**, 8069-8097.
3 I. Roger, M. A. Shipman and M. D. Symes, *Nat. Rev. Chem.*, 2017, **1**, 0003.
4 H. Osgood, S. V. Devaguptapu, H. Xu, J. Cho and G. Wu, *Nano Today*, 2016, **11**, 601-625.
5 M. Gong and H. Dai, *Nano Res.*, 2015, **8**, 23-39.
6 C. C. McCrory, S. Jung, J. C. Peters and T. F. Jaramillo, *J. Am. Chem. Soc.*, 2013, **135**, 16977-16987.
7 S. Cobo, J. Heidkamp, P.-A. Jacques, J. Fize, V. Fourmond, L. Guetaz, B. Jousselme, V. Ivanova, H. Dau and S. Palacin, *Nat. Mater.*, 2012, **11**, 802-807.
8 Y. Wang, Y. Zhang, Z. Liu, C. Xie, S. Feng, D. Liu, M. Shao and S. Wang, *Angew. Chem. Int. Ed.*, 2017, **56**, 5867-5871.
9 R. Liu, Y. Wang, D. Liu, Y. Zou and S. Wang, *Adv. Mater.*, 2017, 1701546.
10 Y. Yang, H. Fei, G. Ruan, C. Xiang and J. M. Tour, *ACS nano*, 2014, **8**, 9518-9523.
11 J. Chang, Y. Xiao, M. Xiao, J. Ge, C. Liu and W. Xing, *ACS Catal.*, 2015, **5**, 6874-6878.
12 D. Li, H. Baydoun, B. Kulikowski and S. L. Brock, *Chem. Mater.*, 2017, **29**, 3048-3054.
13 Q. Liu, J. Jin and J. Zhang, *ACS Appl. Mater. Interfaces*, 2013, **5**, 5002-5008.
14 P. Ganesan, M. Prabu, J. Sanetuntikul and S. Shanmugam, *ACS Catal.*, 2015, **5**, 3625-3637.
15 Y. Liu, H. Cheng, M. Lyu, S. Fan, Q. Liu, W. Zhang, Y. Zhi, C. Wang, C. Xiao and S. Wei, *J. Am. Chem. Soc.*, 2014, **136**, 15670-15675.
16 C. Tang, N. Cheng, Z. Pu, W. Xing and X. Sun, *Angew. Chem. Int. Ed.*, 2015, **54**, 9351-9355.
17 F. Dionigi and P. Strasser, *Adv. Energy Mater.*, 2016, **6**, 1600621.
18 K. Fominykh, P. Chernev, I. Zaharieva, J. Sicklinger, G. Stefanic, M. Döblinger, A. Müller, A. Pokharel, S. Böcklein and C. Scheu, *ACS nano*, 2015, **9**, 5180-5188.
19 L. Trotochaud, S. L. Young, J. K. Ranney and S. W. Boettcher, *J. Am. Chem. Soc.*, 2014, **136**, 6744-6753.
20 S. L. Candelaria, N. M. Bedford, T. J. Woehl, N. S. Rentz, A. R. Showalter, S. Pylypenko, B. A. Bunker, S. Lee, B. Reinhart, Y. Ren, S. P. Ertem, E. B. Coughlin, N. A. Sather, J. L. Horan, A. M. Herring and L. F. Greenlee, *ACS Catal.*, 2017, **7**, 365-379.

This journal is © The Royal Society of Chemistry 20xx

21 J. Chang, L. Liang, C. Li, M. Wang, J. Ge, C. Liu and W. Xing, *Green Chem.*, 2016, **18**, 2287-2295.
22 R. Ge, H. Du, K. Tao, Q. Zhang and L. Chen, *ACS Appl. Mater. Interfaces*, 2017, **9**, 15383-15387.
23 Y. Yang, L. Zhuang, R. Lin, M. Li, X. Xu, T. E. Rufford and Z. Zhu, *J. Power Sources*, 2017, **349**, 68-74.
24 A. Indra, P. W. Menezes, N. R. Sahraie, A. Bergmann, C. Das, M. Tallarida, D. Schmeißer, P. Strasser and M. Driess, *J. Am. Chem. Soc.*, 2014, **136**, 17530-17536.
25 Y. Li and C. Zhao, *Chem. Mater.*, 2016, **28**, 5659-5666.
26 J. Zhang, Y. Hu, D. Liu, Y. Yu and B. Zhang, *Adv. Sci.*, 2017, **4**, 1600343.
27 M. Liu and J. Li, *ACS Appl. Mater. Interfaces*, 2016, **8**, 2158-2165.
28 J. Wang, P. Nie, B. Ding, S. Dong, X. Hao, H. Dou and X. Zhang, *J. Mater. Chem. A*, 2017, **5**, 2411-2428.
29 F. Song and X. Hu, *Nat. Commun.*, 2014, **5**, 4477.
30 S. H. Bae, J. E. Kim, H. Randriamahazaka, S. Y. Moon, J. Y. Park and I. K. Oh, *Adv. Energy Mater.*, 2017, **7**, 1601492.
31 P. He, X. Y. Yu and X. W. D. Lou, *Angew. Chem.*, 2017, **129**, 3955-3958.
32 R. R. Salunkhe, Y. V. Kaneti, J. Kim, J. H. Kim and Y. Yamauchi, *Acc. Chem. Res.*, 2016, **49**, 2796-2806.
33 B. Li, H. M. Wen, Y. Cui, W. Zhou, G. Qian and B. Chen, *Adv. Mater.*, 2016, **28**, 8819–8860.
34 J. Tang, S. Wu, T. Wang, H. Gong, H. Zhang, S. M. Alshehri, T. Ahamad, H. Zhou and Y. Yamauchi, *ACS Appl. Mater. Interfaces*, 2016, **8**, 2796-2804.
35 X. Y. Yu, L. Yu, H. B. Wu and X. W. D. Lou, *Angew. Chem.*, 2015, **127**, 5421-5425.
36 Q. Wang, N. Wang, S. He, J. Zhao, J. Fang and W. Shen, *Dalton Trans.*, 2015, **44**, 12878-12883.
37 X.-Y. Yu, Y. Feng, B. Guan, X. W. D. Lou and U. Paik, *Energy Environ. Sci.*, 2016, **9**, 1246-1250.
38 Y. Zhan, M. Lu, S. Yang, Z. Liu and J. Y. Lee, *ChemElectroChem*, 2016, **3**, 615-621.
39 M. C. Biesinger, B. P. Payne, L. W. Lau, A. Gerson and R. S. C. Smart, *Surf. Interface Anal.*, 2009, **41**, 324-332.
40 J. M. Barforoush, D. T. Jantz, T. E. Seuferling, K. R. Song, L. C. Cummings and K. C. Leonard, *J. Mater. Chem. A*, 2017, **5**, 11661-11670
41 H. Kim, D.-H. Seo, H. Kim, I. Park, J. Hong, K.-Y. Park and K. Kang, *Chem. Mater.*, 2012, **24**, 720-725.
42 Y. Zhan, S. Yang, M. Lu, Z. Liu and J. Y. Lee, *Electrochim. Acta*, 2017, **227**, 310-316.
43 D. Yang, Z. Lu, X. Rui, X. Huang, H. Li, J. Zhu, W. Zhang, Y. M. Lam, H. H. Hng and H. Zhang, *Angew. Chem. Int. Ed.*, 2014, **53**, 9352-9355.
44 X. Ji, L. Cui, D. Liu, S. Hao, J. Liu, F. Qu, Y. Ma, G. Du, A. M. Asiri and X. Sun, *Chem. Commun.*, 2017, **53**, 3070-3073.
45 P. Chen, K. Xu, T. Zhou, Y. Tong, J. Wu, H. Cheng, X. Lu, H. Ding, C. Wu and Y. Xie, *Angew. Chem. Int. Ed.*, 2016, **55**, 2488-2492.
46 S. Dutta, C. Ray, Y. Negishi and T. Pal, *ACS Appl. Mater. Interfaces*, 2017, **9**, 8134-8141.
47 H. S. Ahn and T. D. Tilley, *Adv. Funct. Mater.*, 2013, **23**, 227-233.
48 R. Ge, H. Du, K. Tao, Q. Zhang and L. Chen, *ACS Appl. Mater. Interfaces*, 2017, **9**, 15383-15387.
49 W. Wang, D. Liu, S. Hao, F. Qu, Y. Ma, G. Du, A. M. Asiri, Y. Yao and X. Sun, *Inorg. Chem.*, 2017, **56**, 3131-3135.
50 J. G. McAlpin, Y. Surendranath, M. Dinca, T. A. Stich, S. A. Stoian, W. H. Casey, D. G. Nocera and R. D. Britt, *J. Am. Chem. Soc.*, 2010, **132**, 6882-6883.
51 D. K. Bediako, B. Lassalle-Kaiser, Y. Surendranath, J. Yano, V. K. Yachandra and D. G. Nocera, *J. Am. Chem. Soc.*, 2012, **134**, 6801-6809.
52 K. Jin, J. Park, J. Lee, K. D. Yang, G. K. Pradhan, U. Sim, D. Jeong, H. L. Jang, S. Park and D. Kim, *J. Am. Chem. Soc.*, 2014, **136**, 7435-7443.
53 H. Kim, J. Park, I. Park, K. Jin, S. E. Jerng, S. H. Kim, K. T. Nam and K. Kang, *Nat. Commun.*, 2015, **6**, 8253.
54 M. Yoshida, Y. Mitsutomi, T. Mineo, M. Nagasaka, H. Yuzawa, N. Kosugi and H. Kondoh, *J. Phys. Chem. C*, 2015, **119**, 19279-19286.
55 J. Zhu, Z. Ren, S. Du, Y. Xie, J. Wu, H. Meng, Y. Xue and H. Fu, *Nano Res.*, 2017, **10**, 1819-1831.
56 W. J. Dong, Y. J. Song, H. Yoon, G. H. Jung, K. Kim, S. Kim and J. L. Lee, *Adv. Energy Mater.*, 2017, 1700659.
57 P. Li, Z. Jin, J. Yang, Y. Jin and D. Xiao, *Chem. Mater*, 2016, **28**, 153-161.
58 M. Görlin, J. Ferreira de Araújo, H. Schmies, D. Bernsmeier, S. r. Dresp, M. Gliech, Z. Jusys, P. Chernev, R. Kraehnert and H. Dau, *J. Am. Chem. Soc.*, 2017, **139**, 2070-2082.
59 J. Wang, Z. Wu, L. Han, R. Lin, W. Xiao, C. Xuan, H. L. Xin and D. Wang, *J. Mater. Chem. A*, 2016, **4**, 5678-5684.

Table of contents

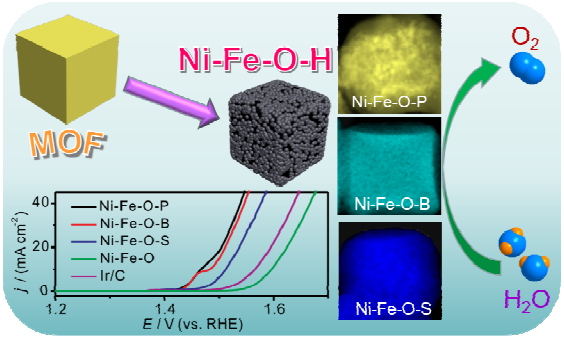

Different heteroatom incorporated NiFe-based nanocubes are synthesized with MOFs as precursors and exhibit enhanced OER activities.